Identification of a new inhibitor of Ran GTPase with therapeutic value in epithelial ovarian cancer

Zied Boudhraa[δ,1,2], Xiaohong Tian[δ,5], Ryhem Gam[ε,1,2], Sabrina Ritch[ε,1,2], Jennifer Kendall-Dupont[1,2], Euridice Carmona[1,2], Diane Provencher[1,2,3], Jian Hui Wu[5], Anne-Marie Mes-Masson[1,2,4*]

[1] Centre de recherche du Centre hospitalier de l'Université de Montréal (CRCHUM), Montreal, Canada.

[2] Institut du cancer de Montréal (ICM), Montreal, Canada.

[3] Division of Gynecologic Oncology, Université de Montréal, Montreal, Canada.

[4] Department of Medicine, Université de Montréal, Montreal, Canada.

[5] Lady Davis Institute, Jewish General Hospital, McGill University, Montreal, Canada

[δ] First Co-authors

[ε] Second Co-authors

[*] **Corresponding author:** Anne-Marie Mes-Masson, CRCHUM, R10-412, 900 rue St-Denis, Montreal, Quebec, Canada, H2X 0A9. Phone: (514) 890-8000 ext. 25496. E-mail: anne-marie.mes-masson@umontreal.ca

ABSTRACT

Accumulated studies suggest that the small GTPase Ran is critical in cancer initiation and progression. Compounds that block Ran activity would be valuable for cancer treatment. Here, by learning lessons from the discovery of KRAS G12C inhibitors, we generated a structural model of the switch II pocket of GDP-bound Ran to identify potential inhibitors of Ran by virtual screening. After *in vitro* verification and hit optimization, we identified chemical compound M36 as an efficient inhibitor of Ran with a therapeutic value. Binding of M36 to Ran was confirmed by cellular thermal shift assay. The specificity of M36 towards Ran was demonstrated by the evaluation of the active GTP-bound forms of a range of GTPases including Ran, RhoA, Cdc42 and Rac1; and by the expression of a dominant active mutant of Ran. Remarkably, similar to depletion of Ran by siRNA, M36 exhibits a specific toxicity in aneuploid ovarian cancer cells and represses DNA repair systems. In accordance with this, we established a synergistic relationship between M36 and the FDA approved PARP inhibitor olaparib. *In vivo*, M36 presents acceptable pharmacokinetic properties and, more importantly, inhibits the tumor growth of an aggressive ovarian xenograft model. Clinically relevant, M36 was able to induce cell death in *ex vivo* EOC patient derived micro-dissected tumors. Overall, our study is the first to provide a small-molecule compound inhibitor of Ran with a therapeutic potential.

20 **INTRODUCTION**

21 Ran (Ras related nuclear protein), a member of the RAS superfamily of small GTPases, is
22 unique among other GTPases owing to its subcellular localization. While other GTPases are
23 found in the cytoplasm and associated to subcellular membranes, Ran is found predominately in
24 the nucleus [1]. Ran has been widely studied for its role in mitosis and nucleo-cytoplasmic
25 shuttling of proteins and RNAs [2]. In comparison with normal tissues, Ran was found to be
26 overexpressed in several cancers including breast, renal, gastric, colon, pancreatic, ovarian and
27 lung cancers [3-10]. Furthermore, within the same cancer, the expression of Ran has been found to
28 be positively correlated with patient outcomes in myeloma, lymphoma, neuroblastoma, renal
29 cell, ovarian and breast carcinomas [4-6,10-14]. It has been reported that Ran is involved in
30 supporting at least three hallmarks of cancer, namely proliferative signaling, resisting cell death
31 and activating pathways that support invasion and metastasis [7,9,11,15-21]. Interestingly, we and
32 others have been reported that the loss of Ran using specific siRNAs is lethal for cancer cells
33 with no or moderate effect in normal cells [7,18,22-24]. This suggests that targeting Ran could
34 achieve a valuable therapeutic index.

35 Epithelial ovarian cancer (EOC) is the most common form of all ovarian cancers and is
36 the most fatal of all gynecological malignancies [25,26]. Histologically, EOCs are subdivided into
37 five subtypes where the high-grade serous carcinoma (HGSC) is overrepresented and rates
38 among the most aggressive [25,27]. EOCs are characterized by extremely high intratumoral
39 heterogeneity that poses specific challenges for therapeutic strategies [28] (Platinum- and taxane-
40 based chemotherapy are the standard first-line therapies of EOC [27,29]). However, despite this
41 heterogeneity, aneuploidy is a hallmark of EOC, particularly of HGSC [28] where the
42 chromosomal stability control gene, *TP53*, is mutated in >90% of cases [30,31]. Thus, targeting
43 aneuploidy would be an avenue to efficiently treat this cancer.

44 Recently, we have shown using EOC models, that the differential sensitivity between
45 normal and cancer cells following the loss of Ran is governed by aneuploidy and genomic
46 instability [23]. In particular, we have reported that induction of aneuploidy in rare diploid EOC
47 cell lines or normal cells renders them highly dependent on Ran. We also established an inverse
48 correlation between Ran and the tumor suppressor NR1D1 and reveal the critical role of
49 Ran/NR1D1 axis in aneuploidy-associated endogenous DNA damage repair. We showed that
50 Ran, through the maturation of miR4472, destabilizes the mRNA of NR1D1 impacting several
51 DNA repair pathways [23]. Loss of Ran was then associated with NR1D1 induction, accumulation
52 of DNA damages and lethality of aneuploid EOC cells. Our findings suggest a synthetic lethal
53 strategy targeting aneuploid cells based on their dependency to Ran. We hypothesize that
54 developing small molecules targeting this GTPase is an attractive therapeutic approach for EOC.
55 To date, despite the availability of Ran's crystal structure [32-36], there is no inhibitor proven to be
56 efficient and specific to Ran. The high affinity of Ran to its cognate GTP (pM range) and the
57 high cellular concentration of GTP (millimolar range), makes the identification of an efficient
58 compound with a GTP-competitive mode of action very difficult, if not impossible.

59 In the present study, inspired by the ground-breaking work of KRAS G12C inhibitors
60 [37,38], we aimed to identify allosteric small molecule inhibitors of Ran. The approach chosen was
61 to target the GDP-bound form of Ran at the switch II pocket, with the hypothesis that this would
62 lock the protein in an inactive state, thereby depleting the active Ran population. To this end, a
63 part of the NCI chemical database (90,000 compounds) was screened virtually. After *in vitro*
64 validation and hit optimization, we identified M36 as a promising inhibitor of Ran. M36 mimics
65 the effect of Ran knock down (KD): specific toxicity in aneuploid cancer cells and significant
66 repression of the DDR process. *In vivo*, M36 is well tolerated by mice at high doses, displays an

67 acceptable pharmacokinetic (PK) pattern and significantly delays tumor growth of a very
68 aggressive EOC xenograft model. At the clinical level, M36 was able to induce cell death in *ex*
69 *vivo* micro-dissected tumors derived from an EOC patient. Furthermore, owing to its ability to
70 repress DNA repair systems, we established a synergistic relationship between M36 and the FDA
71 approved PARP inhibitor olaparib. Overall, our findings suggest a new therapeutic strategy for
72 EOC based on the modulation of Ran activity.

73

74 **RESULTS**

75 ***In silico* and cell-based screenings identified M26 as hit compound for Ran inhibition**

76 Inspired by the ground-breaking work of KRAS G12C inhibitors, which bind KRAS G12C
77 mutant at a pocket nearby switch II (referred to as switch II pocket) [37,38], we aimed to target the
78 GDP-bound form of Ran (RanGDP) at the switch II pocket to 'arrest' Ran at its inactivated state
79 (**Figure 1A**). However, one key feature of the switch II pocket of KRAS G12C is that it exists
80 only when it binds with an inhibitor. Our inspection of the crystal structure of RanGDP (pdb:
81 3ch5) found no pre-formed switch II pocket. We thus decided to construct a structural model of
82 the switch II pocket of RanGDP using the crystal structure of KRAS G12C/Inhibitor complex
83 (pdb: 5v6s) as the template **(Figure 1A)**. Next, a part of the NCI chemical database (90,000
84 compounds) was screened virtually against the RanGDP switch II pocket. Top-ranking
85 compounds identified in this *in silico* screen went through a more in-depth visual inspection for
86 binding modes. A total of 28 compounds were selected for further study as potential Ran
87 inhibitors (**Figures 1B and S1A**). Having previously established that aneuploid EOC cells are
88 more sensitive to the loss of Ran than normal or tumoral diploid cells [23], biological activity was
89 assessed by clonogenic assays (at a single dose of 10 μM) using one aneuploid EOC cell line

90 (TOV112D) and the diploid normal ARPE (ARPE-19) cells **(Figures 1C and S1B)**. The
91 criterion for a positive hit was that the compound did not inhibit the colony formation of the
92 ARPE cells but significantly inhibited the number of colonies formed by the TOV112D cells.
93 Our results show that one compound from the *in silico* screening, M26 **(Figure 1B)**, inhibited
94 colony formation of EOC but not the normal cells **(Figure 1C)**. Furthermore, by analyzing
95 PARP cleavage by Western blot, we found that M26 treatment induced apoptosis in TOV112D
96 cells with no notable effect in ARPE cells **(Figure 1D)**, indicating a differential sensitivity
97 between the diploid and aneuploid cells following M26 treatment. Since our screening was
98 virtual using Ran crystal structure, it was therefore important to determine whether our hit
99 compound was able to inhibit Ran in its biological form. For that, the level of active GTP-bound
100 Ran was evaluated in lysates of EOC cells treated or not with M26 using Ran pull down assays.
101 Our results showed a marked decrease in Ran-GTP level in TOV112D cells incubated with this
102 compound compared to DMSO-treated control cells **(Figure 1E)**. Of note, since the number of
103 cells used in the colony formation assay is lower than that of other cell-based assays, a lower
104 concentration of M26 (or its derivatives, see below) was used in this assay. Collectively, our data
105 identified M26 as a potential inhibitor of Ran with an interesting therapeutic value.

106 **Chemical optimization and cell-based screening identified M36 as a promising inhibitor of**
107 **Ran**

108 Plasma esterases are the major drug-metabolizing enzymes in plasma significantly affecting drug
109 stability *in vivo* [39]. As shown in **Figure 1B**, M26 has three ester groups, which would suggest
110 poor bioavailability of the drug when injected *in vivo*. To overcome this issue and explore
111 preliminary structure-activity relationship, a series of M26-derived compounds, in which the
112 ester groups were replaced by ether groups, were synthetized **(Figures 2A and S2A)**. Our results

113 showed that only compound M36 and its derivative M98, inhibited colony formation of
114 TOV112D cells without affecting the ARPE cells **(Figure S2B)**. Interestingly, M36 but not M33
115 inhibited the activation of Ran comparably to the parent compound, M26 **(Figure S2C)**.
116 Therefore, for the rest of the study we selected M36 **(Figure 2A)** for further characterization.
117 Using Ran pull down assays, the effect of M36 on Ran activation was shown to be dose
118 dependent **(Figure 2B)**. In addition, immunofluorescence studies using an antibody specific to
119 active Ran-GTP showed no detectable levels of Ran-GTP in TOV112D cells treated with M36 as
120 compared to the intense staining of the DMSO-treated cells **(Figure 2C)**. More importantly the
121 direct binding of M36 to RanGTPase was assessed by CETSA, a widely used technique to verify
122 the interaction of a compound with its target protein [40]. In this assay, the thermal stability of Ran
123 was investigated at different temperatures in OV1946 cells treated with different concentrations
124 of M36 or with DMSO **(Figures 2D-E)**. As expected, Ran levels detected by Western-blot
125 decreased with increasing temperatures in controls cells treated with vehicle DMSO. However, a
126 shift in this thermal instability was observed when cells were treated with M36, specially at the
127 concentrations of 100 and 200 μM. Significantly higher levels of Ran were observed at all M36
128 concentrations for temperatures of 58°C, 59°C and 60°C **(Figure 2D)**, indicating M36 engages
129 with Ran and increases its thermal stability. As negative control, we show that this protection
130 was not observed when OV1946 cells were treated with increasing concentrations of the PARP
131 inhibitor Olaparib (**Figure S3A**), a drug known to impact DNA repair [41]. In all, these results
132 indicate that M36 targets Ran and inhibits Ran-GTP activation.

133 Regarding its effect on cancer cells, the IC_{50} value of M36 for the TOV112D cell line as
134 determined by clonogenic assay was found to be 10.02±0.36 μM. Only a minimal effect was
135 observed for the normal ARPE cell line at high concentrations **(Figure 3A)**. To support our

136 observation regarding the differential sensitivity between diploid and aneuploid cells with M36
137 treatment, we expanded our analysis by using, in addition to ARPE and TOV112D cell lines, five
138 aneuploid HGSC cell lines [TOV1946, TOV2295(R), OV1946, OV866(2) and OV4485] and one
139 diploid low-grade serous EOC TOV81D cell line. Proliferation assays were performed on these
140 cell lines after treatment with M36. As a positive control, the same cell lines were transfected
141 with siRan that we have previously characterized for its specificity [21,23]. Remarkably, like siRan,
142 M36 demonstrated a specific toxicity in aneuploid cells with only a moderate effect in normal
143 and EOC diploid cells **(Figure 3B)**. Similarly, this toxicity was accompanied by the induction of
144 apoptosis specifically in aneuploid cells **(Figure 3C)**, highlighting the therapeutic potential of
145 M36. Since aneuploidy and genomic instability are hallmarks of the majority of cancers [42,43], we
146 assessed the toxicity of M36 in other cancer cell lines derived from prostate, gastrointestinal,
147 breast and skin cancers. Strikingly, M36 showed a significant toxicity in all the cell lines tested
148 **(Figure S2D)**. These results suggest that the use of M36 would not be limited to ovarian cancer
149 but could be extended to other tumors. To investigate the specificity of M36 towards Ran, the
150 effect of M36 on the activation of other GTPases (RhoA, Cdc42 and Rac1) was assessed. As
151 shown in **Figure 3D**, no significant effect on the activation of these GTPases was observed when
152 incubated with M36. Furthermore, overexpression of constitutively active (GTP-bound form)
153 Ran^{Q69L} mutant protein [44] mitigated the inhibition of TOV112D cell growth by M36 **(Figure**
154 **3E)**. Together, these data provide evidence of the specificity of M36 towards Ran and indicate
155 that this compound acts specifically on the GDP-bound form of Ran.

156 **M36 mimics the effect of Ran knock down (KD) regarding DDR**

157 We have shown that the differential sensitivity between diploid and aneuploid cells following the
158 loss of Ran comes from the involvement of the Ran/NR1D1 axis in modulating DNA repair [23]. In

159 fact, following the loss of Ran, NR1D1 was induced and in turn repressed several DNA repair
160 pathways including the HR and the NHEJ pathways, leading to the accumulation of DNA
161 damages. We first assessed the effect of M36 on NR1D1 expression. As observed following Ran
162 KD, M36 significantly induced the expression of NR1D1 in two aneuploid EOC cell lines
163 (TOV112D and OV1946) **(Figure 4A-B)**. As negative control, we show that NR1D1 expression
164 was not affected when cells were treated with the PARP inhibitor Olaparib **(Figure S3B)**,
165 suggesting that M36 effect on NR1D1 expression is specific. Next, to investigate whether M36
166 was able to repress the DDR process, TOV112D cells were either transfected with siRan or
167 treated with M36 and the DDR components were analyzed by immunofluorescence.
168 Remarkably, in accordance with Ran KD, M36 treatment induced DNA damage accumulation as
169 shown by an increase of p-γH2AX foci number **(Figure 4C)** and an inhibition of the HR and the
170 NHEJ pathways, which were assessed respectively by the quantification of Rad51 **(Figure 4D)**
171 and 53BP1 **(Figure 4E)** foci formation. Interestingly, since the cytoplasmic staining of 53BP1
172 following M36 treatment was increased **(Figure 4F)**, the inhibition of 53BP1 foci formation by
173 M36 can probably be attributed to the inhibition of the Ran-dependent nuclear import of this
174 protein that has been previously reported [15] and is in accordance with the Ran KD condition
175 **(Figure 4F)**. Collectively, our data demonstrate that M36 mimics the effect of the loss of Ran
176 regarding DDR.

177 **Evaluation of the therapeutic potential of M36 *in vivo***

178 The promising *in vitro* results of M36 led us to initiate *in vivo* analysis of this small molecule
179 inhibitor of Ran. Pharmacokinetic results showed that after a single IP injection (200 mg/kg),
180 plasma levels of M36 was detected at our first time point of 5 minutes, reached a peak at 30
181 minutes (100 μM), remained at around 10 μM after 6 h and is still detectable at 24 h **(Figure**

182 **5A)**. Therefore, M36 displayed an acceptable PK pattern. For the tolerance study, M36 was
183 injected IP daily for a period of three weeks. Our results showed that treated mice continued to
184 gain weight **(Figure 5B)**, suggesting that, even at higher doses (200 mg/kg), M36 was well
185 tolerated. Inhibition of tumor growth was evaluated in the human chemoresistant ovarian cancer
186 xenograft model, TOV112D. As we've previously shown, this xenograft model showed
187 resistance to carboplatin treatment [45]. Furthermore, when mice were treated with the maximum
188 tolerated dose of the PARP inhibitor Olaparib **(Figure 5C)**, no significant effect was observed
189 regarding tumor growth. However, M36 treatment significantly delayed tumor growth of this
190 aggressive model **(Figure 5D-E)** and prolonged mouse survival **(Figure 5F)**, highlighting the
191 promising potential of this compound for the treatment of EOCs, particularly for those that are
192 difficult to treat.

193 **M36 induces cell death in *ex vivo* ovarian cancer models**

194 To evaluate the clinical relevance of M36 treatment, the viability of microdissected tumor
195 samples derived from EOC xenografts or patient samples were evaluated *ex vivo* using our
196 microfluidic methodology [46]. Our results show **(Figure 6)** a significant increase in the intensity
197 of cleaved caspase 3 (CC3) staining 72 hs after M36 treatment in both the OV1946 xenograft and
198 the TOV12018G patient tumor models. For the TOV112D xenograft model, this effect was also
199 observed, but no significance was achieved **(Figure S3B)**, and a 50% decrease in the nuclear Ki-
200 67 staining was observed in this model 24 hs post-treatment. These results suggest that M36
201 induces cell death by apoptosis and could decrease cell proliferation in *ex vivo* EOC models,
202 including patient tumor, further corroborating its therapeutic value.

203 **Combination of M36 and Olaparib triggers synthetic lethality in EOC cells**

204 It is presumed that resistance to PARP inhibitor therapy is closely related to the activation of the
205 HR pathway of cancer cells [47]. Therefore, combination treatments of PARP inhibitor with drugs
206 that inhibit the HR pathway would be promising to circumvent this resistance. Based on our
207 finding that M36 was able to repress the HR pathway, we sought to determine whether M36 was
208 able to sensitize ovarian cancer cells to Olaparib. First, we investigated the effect of M36 on the
209 activation of the HR pathway by Olaparib. Our data in two HR proficient BRCA1/2 wild-type
210 (WT) ovarian cancer cell lines [TOV112D, OV866(2)] showed that M36 efficiently inhibited the
211 induction of the HR pathway (assessed by Rad51 foci quantification) by Olaparib **(Figure 7A)**,
212 and this repression was comparable when irradiation was used as an inducer of this DNA repair
213 pathway **(Figure 4D)**. Next, combination treatments of M36 with Olaparib were undertaken in
214 three BRCA1/2 WT and Olaparib resistant-cell lines, namely TOV112D, OV866(2) and OV90
215 cell lines, together with the normal diploid ARPE cell line. These combinations were performed
216 using increasing concentrations of both drugs (all concentrations used are below the IC_{50}) and
217 evaluated using the Bliss independent model [48], in which values below -1 indicate antagonism,
218 values between -1 and 1 indicate additive effects and values above 1 indicate synergy.
219 Remarkably, in contrast to ARPE cells that did not respond to any combination condition, M36
220 displayed a potent synergistic interaction with Olaparib in all 3 EOC cell lines (Bliss scores
221 ranging from 41.02 to 78.6) **(Figure 7B-D)**. Similarly, while no effect was observed in ARPE
222 cells, M36/Olaparib combination induced a significant increase of cell death in the EOC cell
223 lines in comparison with single treatments, as assessed by FACS using DRAQ7 staining **(Figure**
224 **7E)** and by Western blot using cleaved caspase-3 antibody **(Figure 7F)**. Overall, our data
225 indicate that combining M36 with Olaparib would be an effective combination therapy to
226 counter PARP inhibitor resistance in ovarian cancer.

227

228 **DISCUSSION**

229 The involvement of Ran GTPase in cancer initiation and progression has been discussed for
230 more than a decade [7,8,15-21]. Furthermore, using several *in vitro* and *in vivo* experimental models,
231 Ran has been proposed as a promising therapeutic target of cancer [8,9,14,19,22,23,49]. Recent reports
232 have proposed new strategies to target Ran in the context of cancer therapy. One of them relies
233 on repurposing Pimozide in Ran Targeting [50]. Pimozide was initially identified as a potent
234 antagonist of dopamine receptor D2 (D2R) and used as an antipsychotic drug for the
235 management of schizophrenia and other psychotic disorders. It has been shown that Pimozide
236 inhibits the expression of Ran at the transcriptional level and inhibits breast cancer cell growth *in*
237 *vitro* and *in vivo* [50]. Although this molecule displays an interesting cancer therapeutic value, it is
238 likely that this drug will display severe side effects at the concentrations needed. In fact, it has
239 been shown that mice lacking D2R had impaired motor activity and movement coordination as
240 well as hyperactivity [51]. More importantly, the posology of Pimozide for patients with psychotic
241 disorders is about 0.2 mg/Kg/day, however, in the *in vivo* study proposed for breast cancer
242 therapy, mice were treated daily with Pimozide at 20 mg/Kg/day in order to have a significant
243 effect on tumor growth [50]. These very high doses of Pimozide will inevitably be an issue in the
244 exploration of this drug in the context of cancer. Another strategy relies on Nano-encapsulation
245 technology (using PLGA-based nanoparticles) of a shRNA targeting Ran [52] or a peptide
246 inhibiting the activation of this GTPase by disrupting the interaction between Ran and RCC1
247 [53,54]. Such an approach presents many obstacles making its use in clinic very difficult. First, upon
248 entering the circulation, nanoparticles are often coated with opsonin proteins leading to their
249 clearance by macrophages and affecting their pharmacokinetic properties [55]. Second, blood

250 vessels are leaky with fenestrations ranging between 0.2 and 1.2 μm. Since nanoparticles exist in
251 a range of sizes, it is thought that the size of therapeutic nanoparticles should be well below 200
252 nm [55,56]. However, the NPs used for Ran targeting have a mean diameter of 182–277 nm [53].

253 Here, we aimed to target Ran directly with a new small molecule inhibitor. To date, there
254 is no available drug specific to Ran. One reason for this is the high intracellular concentration of
255 GTP as well as the high affinity of GTP to its cognate GTPase, making the development of an
256 efficient competitor of GTP difficult. Alternatively, it is thought that developing allosteric
257 compounds able to interact with a given GTPase in its GDP-bound form and to lock it on its
258 inactive state is more convenient to attenuate GTPase activity. Inspired by the work of KRAS
259 G12C inhibitors, which bind KRAS G12C mutant at the switch II pocket [37,38], we aimed to target
260 the RanGDP at the switch II pocket to 'arrest' Ran at its inactivated state. However, our
261 inspection of the crystal structure of RanGDP (pdb: 3ch5) found no pre-formed switch II pocket.
262 We thus constructed a structural model of RanGDP switch II pocket by homology modeling and
263 performed in silico screening against the switch II pocket. Chemical optimization of our initial
264 hit M26 lead to compound M36 as a novel Ran inhibitor. Importantly, M36 displays, *in vitro,* a
265 very interesting therapeutic index between normal/diploid and cancer/aneuploid cells that is in
266 alignment with our *in vivo* data. In fact, at higher doses, M36 is well tolerated by mice and
267 exhibits a significant toxicity for one of the most aggressive xenograft models, TOV112D, that
268 do not respond to conventional treatments such as Carboplatin and Olaparib therapies.
269 Furthermore, at the clinical level, M36 was able to induce cell death by apoptosis in *ex vivo*
270 micro-dissected tumors derived from an EOC patient. Another advantage of allosteric inhibitors
271 is that they bind to less conserved sites across GTPases and kinases ensuring specificity and
272 avoiding potential severe side effects [57]. In this regard, we have shown that M36 does not

273 influence the activation of other GTPases such as RhoA, Cdc42 and Rac1. More importantly,
274 overexpression of a dominant active of Ran rescued the toxicity of M36 highlighting the
275 specificity of our Ran inhibitor.

276 Olaparib has shown promising results for HGSC treatment and was recently approved by
277 the FDA as maintenance therapy for patients harboring BRCA1/2 mutations (HR deficient) [58].
278 This stratification comes from the observation that HR activation is closely linked to non-
279 responsiveness and resistance to PARP inhibitor therapy [47]. Therefore, combination treatment of
280 a PARP inhibitor with drugs that inhibit the HR pathway is actively being exploited in the
281 clinical setting [59,60], and might be effective to induce lethality in HGSC cells. Here, we have
282 shown that M36 induced HR deficiency and dramatically sensitized three BRCA1/2 WT and
283 Olaparib resistant cell lines (TOV112D, OV866(2) and OV90 [61]) to PARP inhibitor therapy.
284 This result is of great interest since it could open new perspectives to circumvent resistance, and
285 possibly to expand PARP inhibitor therapy to patients that are currently excluded. Many cancers
286 are characterized by widespread aneuploidy and genomic instability [42,43]. Hence, targeting these
287 hallmarks would be effective for the development of a new targeted therapy, not only for EOC,
288 but also for a variety of cancers. In our previous work, we have shown that targeting Ran is an
289 effective way to eliminate cancer cells with chromosomal and genomic instability [23]. This
290 prompted us to investigate the therapeutic value of M36 in other cancers. Interestingly, we found
291 that M36 is also toxic in a range of cancer models including prostate, gastrointestinal, breast and
292 skin cancers. These results are encouraging and in future studies we plan to investigate the *in*
293 *vivo* efficacy of M36 in these models.

294 In conclusion, though further medicinal chemistry optimization is required, our study is
295 the first to provide the generation of a first-in-class compound inhibitor of Ran with a therapeutic
296 potential for cancer in general and EOC in particular.
297

298 **ONLINE METHODS**

299 **Computational modeling and in silico screening**

300 The structural model of RanGDP with switch II pocket was built using crystal structure of
301 RanGDP (pdb: 3ch5) and crystal structure of KRAS G12C in complex with an inhibitor at switch
302 II pocket (pdb: 5v6s) as the templates, by software Modeller (UCSF, CA, USA). Among the 200
303 models generated, the model with lowest objective function was selected for further work.
304 90,000 compounds from NCI-open database were virtually screened against the switch II pocket
305 of the RanGDP model, using software GOLD (The Cambridge Crystallographic Data Centre,
306 Cambridge, UK).

307 **Medicinal chemistry**

308 28 top-ranking candidate compounds were kindly provided, as a gift, by the Drug Synthesis and
309 Chemistry Branch, Developmental Therapeutics Program, NCI, Bethesda, MD, USA. Initial hit
310 M26 was re-synthesized and characterized by NMR analysis. Chemical optimization of M26,
311 leading to compound M36, is described in the supplemental information.

312 **Cell lines and cell culture**

313 The human EOC cell lines used [TOV81D, TOV112D, OV90, OV866(2), TOV1946, OV1946,
314 TOV2295(R), OV4485] were derived in our laboratory from patients' tumors (TOV) or ascites
315 (OV) [62-65]. All EOC cell lines were maintained in low oxygen at 7% O_2 and 5% CO_2 and grown
316 in OSE medium (Wisent, Montreal, QC) supplemented with 10% FBS (Wisent), 0.5 µg/mL

317 amphotericin B (Wisent) and 50 μg/mL gentamicin (Life Technologies Inc., Burlington, ON).
318 The human retinal epithelial cell line ARPE (ARPE-19) was purchased from American Type
319 Culture Collection (ATCC, Manassas, VA) and maintained in DMEM-F12 (Wisent) medium
320 supplemented with 10% FBS (Wisent), 0.5 μg/mL amphotericin B (Wisent) and 50 μg/mL
321 gentamicin (Life Technologies Inc.).

322 **Small interference RNA (siRNA) treatment**

323 Suspensions of 10^6 cells in 100 μL of nucleofector solution V (Lonza Group Ltd, Basel,
324 Switzerland) were transfected by electroporation with 1.2 nmoles siRNA targeting Ran (J-
325 010353-06, ON-TARGETplus, Dharmacon Thermo Fisher Scientific Inc., Waltham, MA). For
326 each experiment, efficiency of Ran silencing was verified 48 hours after transfection by Western
327 blot analysis. Scramble siRNA (D-001810-02, Dharmacon) was used as a control in all
328 experiments.

329 **Clonogenic survival**

330 Clonogenic assays were performed as previously described [61]. Colonies were counted under a
331 stereo microscope and reported as percent of control. IC_{50} values were determined using Graph
332 Pad Prism 5 software (GraphPad Software Inc., San Diego, CA). Each experiment was
333 performed in duplicate and repeated three times. Sensitivity of the cell lines to small molecule
334 inhibitors of Ran was assessed using a concentration range of 0–40 μM.

335 **IncuCyte cell proliferation phase-contrast imaging assay**

336 Cells (2,000 cells/well) were plated in a 96-well plate. The next day, compounds were added at
337 the indicated concentrations. Following treatment, cell confluence was imaged by phase contrast
338 using the IncuCyte live cell monitoring system (Essen BioScience, Ann Arbor, MI). Frames were
339 captured at day 0 (immediately after treatment) and at the end of the experiment using a 10X

340 objective. For Ran KD experiments, cells were seeded in a 96-well plate (4,000 cells/well)
341 directly after transfection. Cell confluence monitoring started the next day as described above.

342 **Protein preparation and western blot analysis**

343 Cells were lysed with RIPA buffer containing protease inhibitors. Whole cell lysates were run
344 through a Bradford assay (Thermo Fisher Scientific) for protein quantification. Around 25–50
345 µg of protein was separated by 12.5% SDS-PAGE and transferred onto nitrocellulose
346 membranes. The resultant blots were probed with Ran (1:10 000, sc-271376 Santa Cruz
347 Biotechnology, Dallas, TX), cleaved PARP (1:1000, #9541, Cell Signaling Technology Inc.,
348 Danvers, MA), cleaved caspase 3 (1:1000, #9661, Cell Signaling Technology Inc.), GAPDH
349 (1:2500, #2118, Cell Signaling Technology Inc.) or beta-actin (1:50 000, ab6276, Abcam Inc.,
350 Toronto, ON, Canada) primary antibodies overnight at 4°C then with peroxidase-conjugated
351 secondary antibodies for 2 hours at room temperature. Proteins were detected using enhanced
352 chemiluminescence (Thermo Fisher Scientific).

353 **RT-PCR**

354 The total RNA from TOV-112D or OV1946 cells was isolated using RNeasy Kit (Qiagen®).
355 The total RNA concentration and purity were measured on a NanoDrop™ spectrophotometer.
356 RNA was reverse transcribed using the QuantiTect Reverse Transcription Kit (Qiagen®)
357 according to the manufacturer's protocol. cDNA amplification was performed with SYBR Green
358 PCR master mix (Applied Biosystems®) using the StepOnePlus Real-Time PCR system
359 (Applied Biosystem®). Negative controls were included in all experiments, and actin served as
360 the housekeeping gene. Primers were ordered from Integrated DNA Technologies, Inc:

361 NR1D1:
362 Forward primer: TGGACTCCAACAACAACACAG
363 Reverse primer: GATGGTGGGAAGTAGGTGGG
364 β-actin:

365 Forward primer: CATGTACGTTGCTATCCAGGC
366 Reverse primer: CTCCTTAATGTCACGCACGAT

367 **Cell death analysis by flow cytometry**

368 Cells were treated with M36. Six days after treatment, adherent and floating cells were mixed
369 and incubated 5 minutes at room temperature with DRAQ 7 (ab109202, Abcam Inc). A
370 maximum of 30,000 events were counted per condition using the Fortessa flow cytometer (BD
371 Biosciences, Mississauga, ON) and analyzed with the FlowJo software.

372 **Immunofluorescence**

373 M36-treated and control cells grown on coverslips were washed with 1X PBS, fixed in 4%
374 paraformaldehyde and permeabilized with 0.25% Triton X-100 (Sigma-Aldrich Inc.). After
375 blocking (4% BSA and 4% FBS in PBS), coverslips were incubated with anti–RanGTP (26915,
376 NewEastBioscences, diluted 1:100), anti p-γ-H2AX (Ser139) (05-636, EMD Millipore, diluted
377 1:2000), anti-Rad51 (ab213, Abcam, diluted 1:750), anti 53BP1 (NB100-305, Novus
378 Biologicals, diluted 1:2500) and anti-Geminin (10802-1-AP, Proteintech, diluted 1:1000)
379 antibodies in blocking buffer for 2 hours at room temperature. Subsequently, samples were
380 incubated with Cy-5 (1:500, Life Technologies Inc.) and Alexa Fluor 488 (for Geminin)
381 secondary antibodies for 1 hour. Coverslips were mounted onto slides using Prolong® Gold anti-
382 fade reagent with DAPI (Life Technologies Inc.). Images were obtained using a Zeiss
383 microscope (Zeiss observer Z1) with a 20X objective. For Rad51 and 53BP1 analysis, cells were
384 transfected with siRan or treated with M36 for 48 hours then gamma-irradiated at 10 Gy and
385 fixed one hour after irradiation. Automated analysis software from Zeiss (AxioVision™, Carl
386 Zeiss) was used for foci counting. In each condition, γ-H2AX, Rad51 and 53BP1 foci were
387 quantified in roughly 400 nuclei.

388 **Cellular Thermal Shift Assay (CETSA)**

389 OV1946 cells (10^7 cells/petri) were seeded in 100 mm × 15 mm petri dish and allowed to attach
390 for 24 h. Then, cells were treated with DMSO or M36 at concentrations from 50 to 200 μM and
391 incubated for 1 h at 37 °C. After incubation, cells were washed, trypsinized and centrifuged for 5
392 minutes at 1200 rpm. Cells were resuspended in HBSS, divided into different aliquots and heated
393 for three minutes at different temperatures using the Biometra TOne PCR (Analytikjena, Jena,
394 Germany). Cell lysates were then obtained by three freeze-thaw cycles in liquid nitrogen (1 min
395 each step of each cycle) followed by centrifugation at 20,000 × g for 20 min at 4°C. The
396 supernatants were harvested, and SDS-PAGE loading buffer was added before boiling for 5min.
397 Proteins were migrated and blotted into PVDF membranes. Primary antibodies used were: Ran
398 (ab53775, Abcam, 1/5000) and β-Actin (ab6276, Abcam, 1/5000). Proteins were detected by
399 HRP-secondary antibody and the ECL detection kit (Clarity and Clarity Max ECL Western
400 Blotting Substrates from Biorad). Densitometry analyses were conducted using the UV-VIS
401 Spectrophotometer (Thermo Fisher Scientific) and relative intensity of Ran protein was obtained
402 by the ratio over the β-actin band.

403 **Ran, Cdc42, RhoA and Rac1 activation assays**

404 Cells were seeded onto 6-well tissue culture plates in such a way that cell confluence reached
405 approximately 70% the day of the experiment. The day of the experiment cells were treated for 1
406 hour with the indicated compounds prior to protein extraction and quantification. Assays were
407 performed using the Ran, Rac1 activation assay kits (Cell Biolabs) and the RhoA and Cdc42 G-
408 LISA activation assay kits (Cytoskeleton®) according to the manufacturer recommendations.

409 ***In vivo* study**

410 For the PK studies, 6-week-old female CD1 mice (Charles River laboratories, Senneville, QC,
411 Canada) received a single intraperitoneal injection of M36 (200 mg/kg), dissolved in DMSO

412 10%, Kolliphor® EL 10%, PEG-400 20% and PBS 60%. For each time point (5, 30, 120, 240,
413 360 and 1440 minutes), 3 mice were sacrificed and blood was collected by cardiac puncture.
414 Plasma levels of the compound were measured by mass spectrometry. For the tolerance test,
415 M36 was dissolved as described above and injected intraperitoneally into 6-week-old female
416 NOD.Cg-Rag1^{tm1Mom}Il2rg^{tm1Wjl}/SzJ (NRG) female mice (The Jackson laboratory, Bar Harbor,
417 ME) every day (except on weekends) at 200 mg/kg. During this study, mice were monitored for
418 survival and weight loss/gain. For the tumor xenograft experiment, NRG mice were injected with
419 10^6 TOV112D cells suspended in a mix of 1:1 PBS and matrigel (BD Biosciences) at
420 subcutaneous sites. Treatments with M36 started the following day. Measurements of tumor size
421 were collected at least twice a week until tumors reached limit points (2000 mm3). All animal
422 procedures were performed in accordance with the guidelines for the Care and Use of Laboratory
423 Animals of the CRCHUM and were approved by the Comité institutionnel de protection des
424 animaux (CIPA) (Protocols #C18009AMMs and C22014AMMs).

425 **Micro-dissected tissue (MDT) production, culture and treatment**

426 MDTs were obtained from both ovarian cancer cell xenografts or patient tissue samples. For the
427 xenografts, cell suspensions containing $1x10^6$ cells for TOV112D or $5x10^6$ cells for OV1946 in
428 PBS-Matrigel were injected subcutaneously in NRG female mice. Solid tumours were harvested
429 at volumes between 800 and 1500 mm^3. For patient tissue, samples were collected from patients
430 following informed consent from the Centre hospitalier de l'Université de Montréal (CHUM),
431 Division of Gynecologic Oncology. Samples were processed immediately upon retrieval. The
432 use of human samples was approved by the Comité d'éthique de la recherche du CHUM (CÉR-
433 CHUM, Protocol #BD 04.002).

434 The micro-dissection and loading procedures were adapted from previously published work [46,66].
435 Briefly, both xenograft and patient tumours were sliced into 1cm slices using a scalpel and
436 processed into 350µm slices using a McIlwain™ tissue chopper (Ted Pella©). Tissue slices were
437 kept in Hank's balanced salt solution (HBSS, Wisent) supplemented with 10% FBS, 55 µg/mL
438 of gentamicin and 0.6 µg/mL of amphotericin B. A 500 µm biopsy punch (PUN0500, Zivic
439 instruments) was then used to produce MDTs, spheroidal tissue of approximately 300 µm in
440 diameter. The loading and trapping of MDTs in microfluidic devices were performed as
441 previously described [46]. MDTs were cultured in OSE (xenografts) or Ovarian TumorMACS™
442 (MILTENYI BIOTEC; patient samples) media supplemented with 10% FBS, 55 ug/mL of
443 gentamicin and 0.6 ug/mL of amphotericin B.
444 MDTs were treated with either 100 or 200 µM of M36 in 1% DMSO (Sigma) for 24 or 72hrs
445 continuously. MDTs were then fixed with 10% formalin (Chaptec) and processed following a
446 previously published paraffin-embedding lithography procedure to create micro-dissected tissue
447 microarray (MDTMA) blocks [46].

448 **MDT Immunofluorescence staining and quantification**

449 MDTMA blocks were cut into 4µm sections and put on Matsunami TOMO® hydrophilic
450 adhesion slides (VWR). Slides were stained for KI67 and cleaved-caspase 3 (CC3) to assess
451 proliferation and cell death, respectively, using the *Discovery Ultra* automated stainer (Ventana
452 Medical System inc. (VMSI)). A pan-cytokeratin (CK) antibody was also used to identify the
453 tumour epithelium of the MDTs. Slides were heated at 60˚C for 20 min before staining. Antigen
454 retrieval was carried out with Cell Conditioning 1 solution (VMSI) for 90 min. Mouse anti-KI67
455 (1:500) (9449S, Cell Signaling), rabbit anti-CC3 (1:200) (9661S, Cell Signaling) and guinea pig
456 anti-pan-CK (1:200) (BP5069, Cedarlane) antibodies were dispensed automatically and slides

457 were incubated for 60 minutes at 37˚C. Secondary antibodies, including anti-mouse Alexa 488
458 (1:250) (A-11001, Life Technologies), anti-rabbit Alexa 750 (1:200) (A-21039, Life
459 Technologies) and anti-guinea pig Alexa 647 (1:200) (706-605-148, Cedarlane) were also
460 dispensed automatically and slides were incubated for 60 minutes at 37˚C. A mounting medium
461 with DAPI (MJS Biolynx inc) was used to stain the nuclei. Slides were scanned at 20x with
462 either an Olympus BX61 (Olympus) or an Aperio Versa 200 (Leica) microscope. IF filters used
463 for DAPI, KI67, CC3 and tumour epithelium were DAPI, Alexa-488, Cy7 and Cy5, respectively.
464 Stained MDTs were quantified using the VisiomorphDP software (VisioPharm, Denmark,
465 http://visiopharm.com). Percent of CC3 staining or nuclear K-67 staining in the cytokeratin
466 positive area were quantified and plotted as bar graphs.

467 **Statistical analysis**

468 Data from at least three independent experiments are presented as the means ± SD. Statistical
469 analyses were done using GraphPad Prism version 10 (GraphPad Sofware Inc., http://
470 graphpad.com). Comparisons were carried out using Student's t-test. Analysis of MDTs was
471 done using Two-way ANOVA followed by Tukey's test. Comparisons of survival curves were
472 performed using log-rank test. A p-value of less than 0.05 was considered statistically
473 significant.

474

475 **ACKNOWLEDGMENTS**

476 We thank Kim Leclerc Désaulniers and Lise Portelance for technical assistances with the animal
477 experiments and biobank specimen procurement, respectively. We acknowledge the CRCHUM
478 animal facility, the ICM Imaging/Live Imaging platform, the Molecular Pathology core facility
479 of the CRCHUM and the CRCHUM Microfluidic platform. A-MM-M and DP are researchers of

the CRCHUM/ICM, which receive support from the Fonds de recherche du Québec – Santé (FRQS). ZB was supported by a MITACS fellowship and by the ICM NathalieMoreau Bursary. SR was supported by a studentship from the Canderel Fund of the Institut du cancer de Montréal (ICM).

FUNDING

This work was supported by the Canadian Institute for Health Research (CIHR MOP142724 and PJT148642), the Oncopole in collaboration with the FRQS, the Cancer Research Society, Génome Québec and IRICoR (#265877), and the ICM (Fonds Défi Spyder and Anne-Marie Chagnon). Cell lines as well as patient tissue samples used in this study were provided by the CRCHUM ovarian tumor bank, which is supported by Ovarian Cancer Canada (OCC) and by the Banque de tissus et de données of the Réseau de recherche sur le cancer (RRCancer) of the FRQS affiliated with the Canadian Tumor Repository Network (CTRNet).

AUTHOR CONTRIBUTIONS

ZB, XT, EC, JHW and A-MM-M designed the study. ZB, XT, SR, RG and JK-D performed the experiments. ZB, XT, EC, SR, RG and JK-D analyzed the data. ZB and XT wrote the manuscript. EC, JHW, DP, and A-MM-M supervised the study, provided guidance, and edited the manuscript.

FIGURES

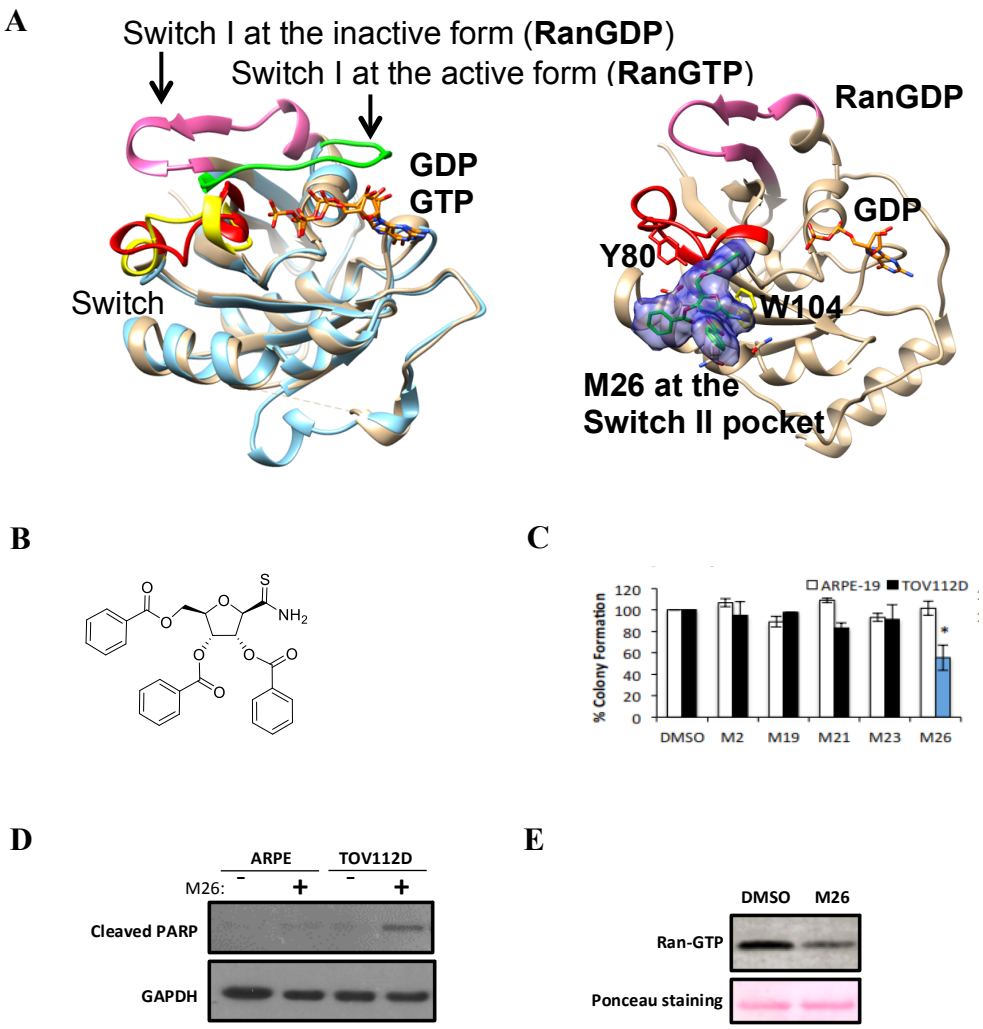

503

504 **Figure 1: *In silico* and cell-based screenings identified M26 as a hit compound for Ran**
505 **inhibition.**

506 **(A)** Left side: Crystal structure of RanGDP (pdb: 3ch5) was aligned to RanGTP (pdb: 3nc1),
507 showing different conformations of Switch I at the activated and inactivated states; Right side:
508 Structural model of the switch II pocket of RanGDP was built by homology modeling and the
509 predicted binding mode of M26 (green sticks with blue surface) at the switch II pocket of
510 RanGDP was showed. **(B)** Chemical structure of M26. **(C)** Colony formation inhibition by
511 selected M compounds at 10 μM in normal ARPE and EOC TOV112D cells. Only the
512 compound M26 inhibited TOV112D without affecting ARPE (blue bar). Bars represent

513 percentage of colonies formed compared to DMSO-treated controls. **(D)** ARPE and TOV112D
514 cells were incubated with M26 (40 μM) to evaluate apoptosis (6 days after treatment) by western
515 blot using the antibody anti-cleaved PARP. **(E)** TOV112D cells were incubated for one hour
516 with M26 (50 μM) before performing RanGTP Pull-down assay on the resultant cell extract.
517

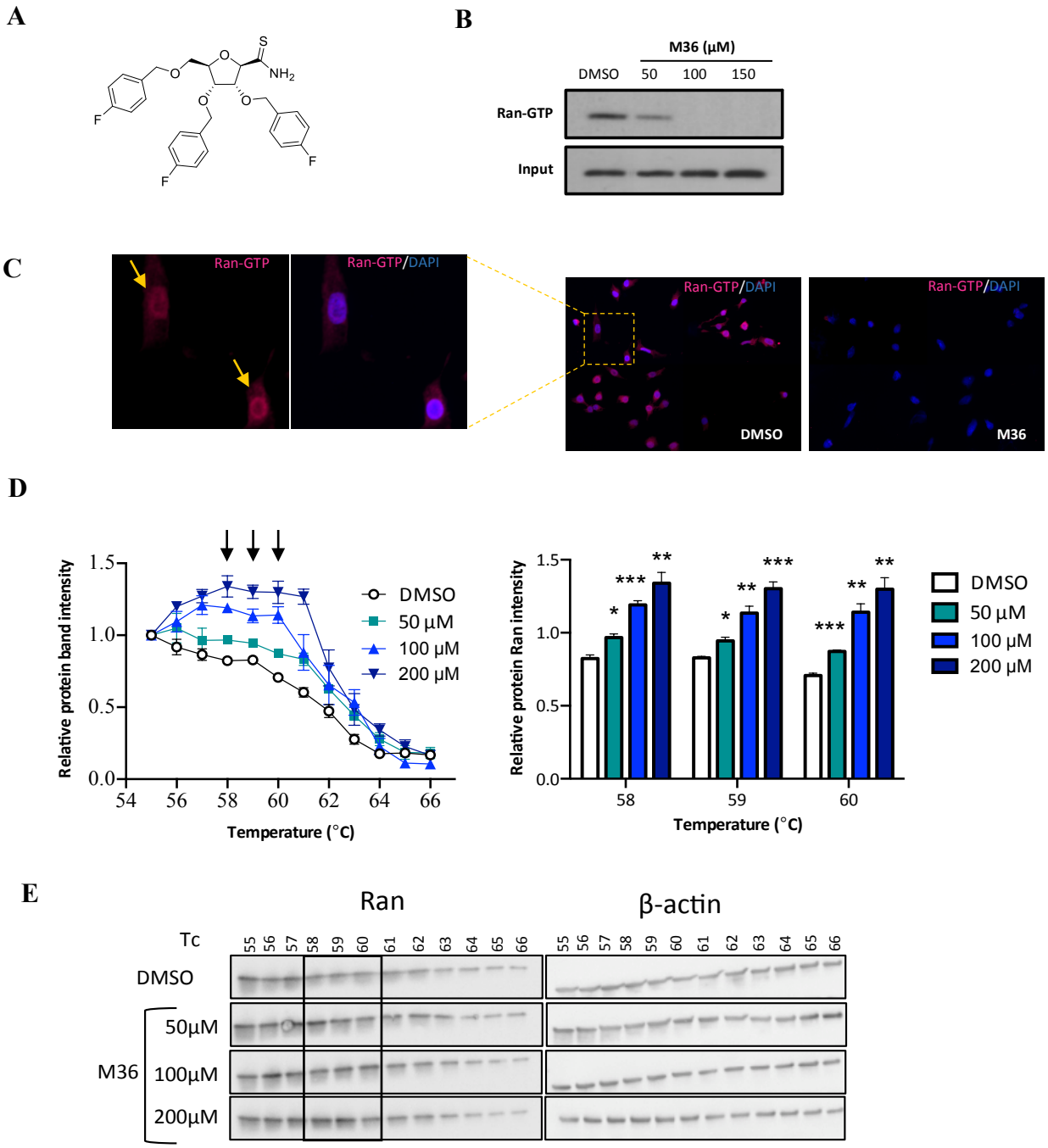

518

519 **Figure 2: M36, a derivative of M26, binds and impacts Ran activation in EOC cells**

520 **(A)** Chemical structure of M36. **(B)** TOV112D cells were treated for one hour with increasing

521 concentrations of M36. Subsequently, RanGTP pull-down assay was performed to assess Ran

522 activation. **(C)** TOV112D cells were treated with M36 (100 μM) for one hour. After cell fixation

523 and permeabilization, RanGTP was revealed by immunofluorescence using a specific antibody
524 (pink). Nuclei are shown by Dapi staining (blue). **(D)** OV1946 cells were treated with M36 (50,
525 100, 200 μM) or DMSO for one hour. CETSA was performed after heating the cell suspensions
526 at different temperatures for three minutes. Cell lysates were subjected to Western blot for
527 evaluation of Ran levels. Data points are densitometry values relative to ß-actin control and
528 normalized to the levels obtained at the lowest temperature used. Arrows indicate the
529 temperatures where significant values were obtained with all three M36 concentrations when
530 compared to control DMSO (as illustrated in the bar graph). *$P < 0.05$ **$P < 0.01$ *** $P < 0.001$
531 ($n = 3$, Student's t-test). **(E)** Representative images of the Western Blots; black rectangular box
532 encompasses the results obtained with the three above-mentioned temperatures.
533

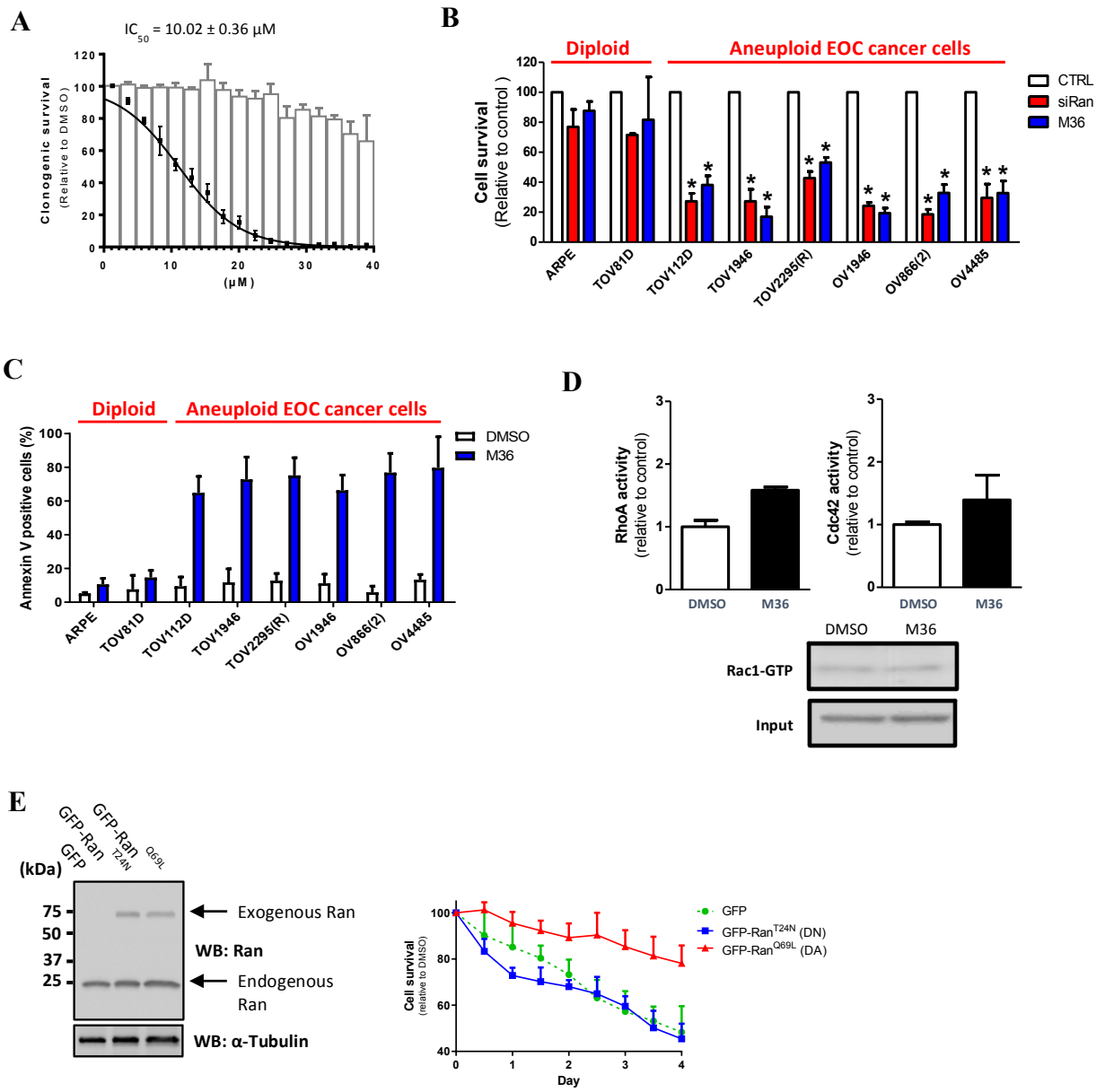

Figure 3: M36 shows selectivity for aneuploid cells and does not interferes with the activation of other GTPases.

(A) Clonogenic assay using different concentrations of M36 in ARPE and TOV112D cells. IC_{50} value was calculated for the TOV112D cells. Bars and curve points represent percentage of colonies formed compared to DMSO-treated controls. **(B)** different EOC cell lines and the

540 normal ARPE cells were transfected with a siRNA targeting Ran or with M36 (40 μM) before
541 assessing cell proliferation using the live cell imaging IncuCyte system. Data are expressed as
542 the percentage of control cells at the end of experiment (96 h) and are representative of at least
543 three independent experiments. **(C)** ARPE and EOC cells were treated with M36 (40 μM) for 6
544 days and then cell death was assessed by FACS using DRAQ7 staining. **(D)** TOV112D cells
545 were treated for one hour with M36 (50 μM) in order to evaluate RhoA (left), Cdc42 (right) and
546 Rac1 (bottom) activities. **(E)** Immunoblots showing successful overexpression in TOV112D
547 cells of dominant active Ran^{Q69L} and dominant negative Ran^{T24N} (left panel). These cells were
548 treated with M36 and cell proliferation was assessed using the live cell imaging IncuCyte system
549 (right panel). Data are expressed as the percentage of DMSO treated cells. *$P < 0.05$ ($n \geq 3$,
550 Student's t-test).
551

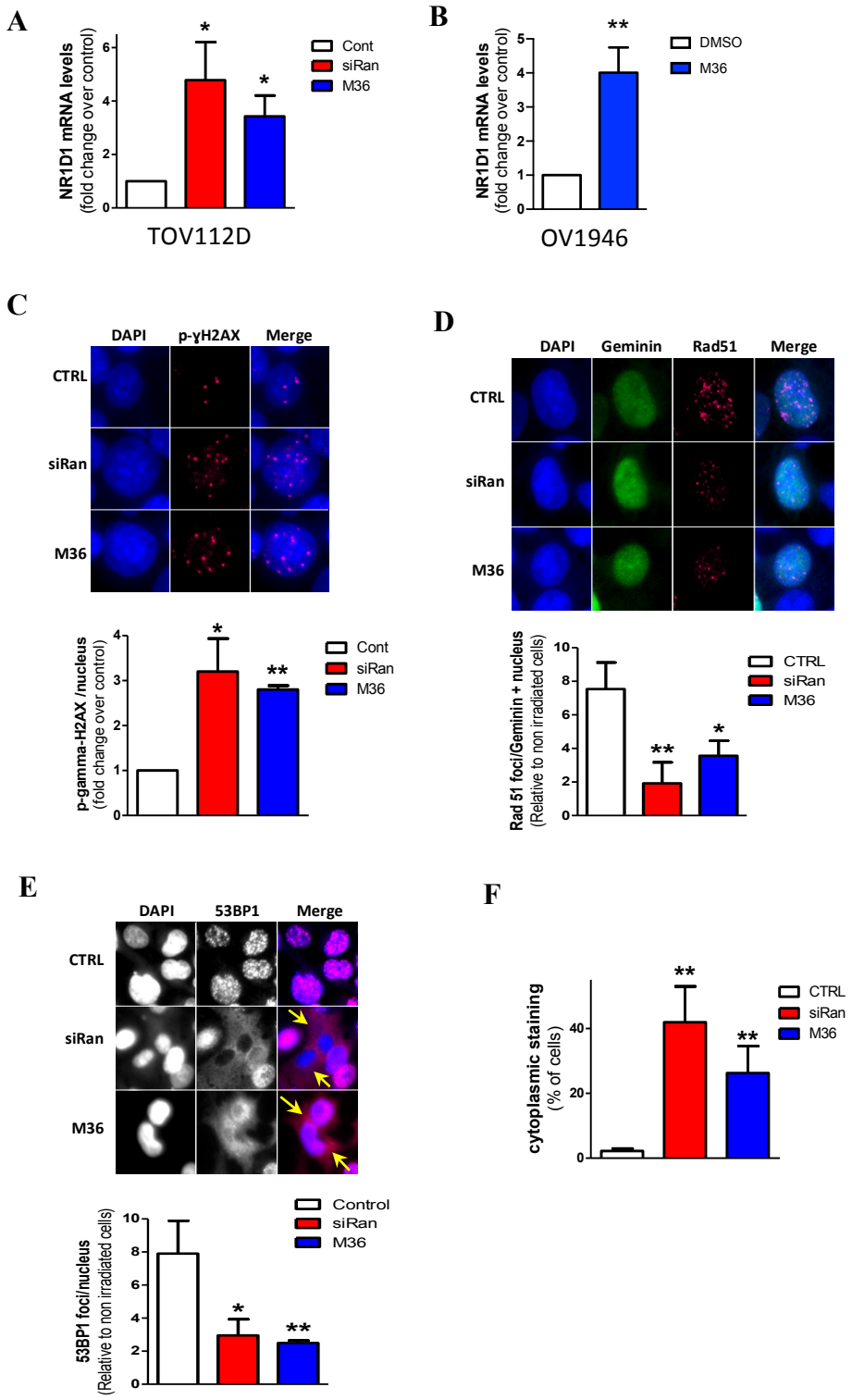

552

553 **Figure 4: M36 mimics the effect of Ran KD regarding DDR**

554 **(A)** The expression of NR1D1 was evaluated by qRT-PCR in TOV112D cells transfected with
555 siRan or treated with M36 (40 μM). **(B)** OV1946 cells were treated with M36 (50 μM) and
556 expression of NR1D1 was evaluated by qRT-PCR. **(C-E)** TOV112D cells were treated with
557 siRan or M36 (20 μM) and allowed to grow for 72 hours. For p-γH2AX staining **(C)**, cells were
558 fixed and stained. For Rad51 **(D)** and 53BP1 **(E)** staining, cells were gamma-irradiated at 10 Gy
559 and fixed 1 hour after irradiation. Representative images after irradiation **(upper panel)** and
560 quantitative analyses of foci formation **(lower panel)** are presented. For Rad51 and 53BP1 foci,
561 data are expressed as the ratio between foci number after and before irradiation. **(F)** Images
562 obtained from **(E)** were used to quantify cells presenting cytoplasmic staining of 53BP1. *$P < 0.05$ **$P < 0.01$ ($n \geq 3$, Student's t-test).
563
564

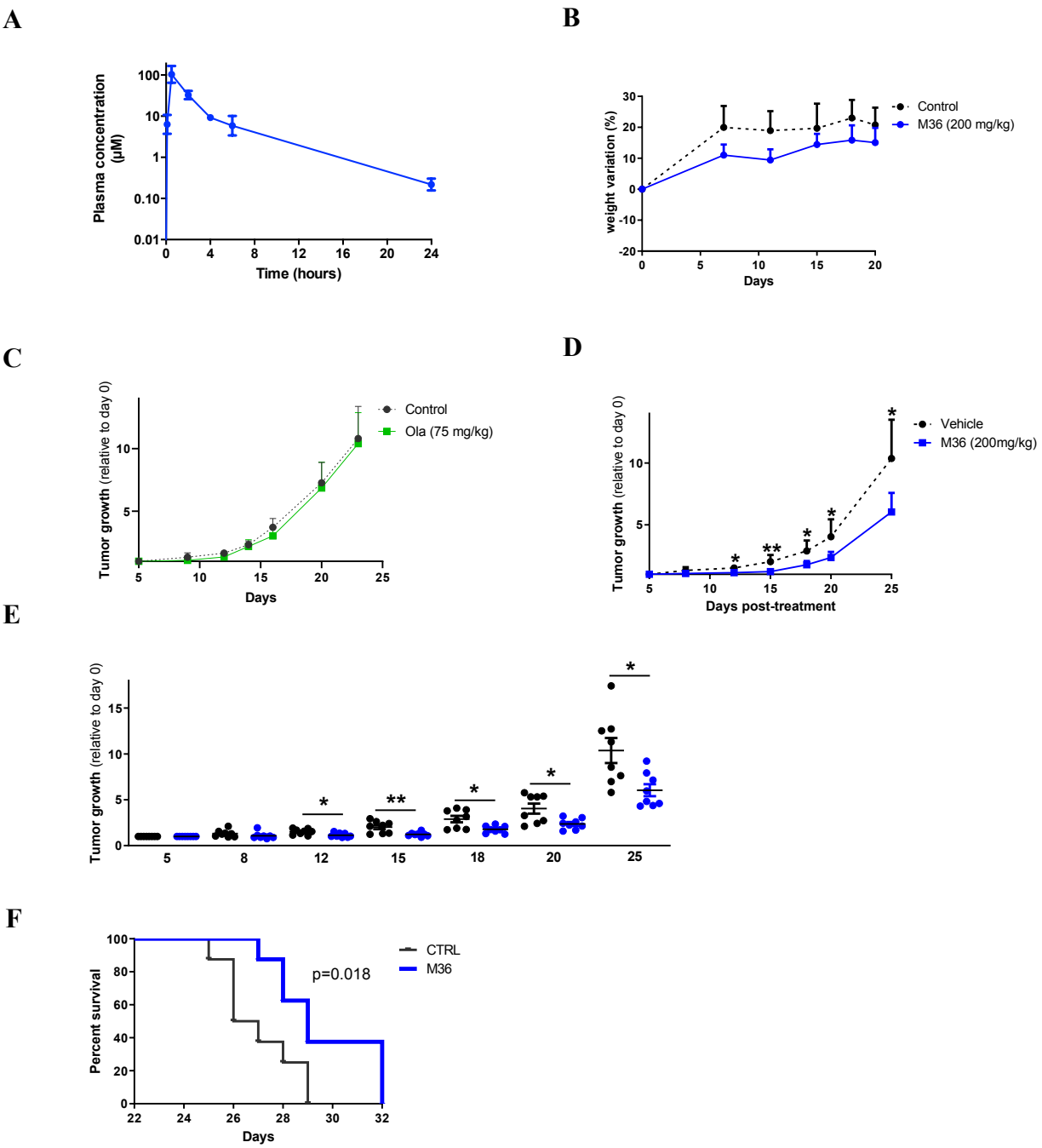

565

566 **Figure 5: Evaluation of the therapeutic potential of M36 *in vivo***

567 **(A)** Measurements of plasma levels of M36 compound after a single intraperitoneal injection

568 (200 mg/kg) in CD1 mice. **(B)** M36 (200 mg/kg) was injected IP daily in NRG mice for 3 weeks.

569 Mouse weight was measured at the indicated time points and expressed as the percentage of their

570 weight on the day of the first injection. **(C-D)** TOV112D cells were subcutaneously injected in
571 NRG mice and treatments with Olaparib (75 mg/kg, daily) **(C)**, and M36 (200 mg/kg, daily) **(D)**
572 were performed. Data are normalized with the mean of tumor size at the first day of injection.
573 **(E)** Tumor growth in individual mice treated with M36 is shown. **(F)** Kaplan-Meier survival
574 curve of mice from **(E)**. In **(D)** and **(E)** data were analyzed using the two-tail Student's t test. In
575 **(F)**, data were analyzed using the Log rank test. *$P < 0.05$, **$P < 0.01$.
576

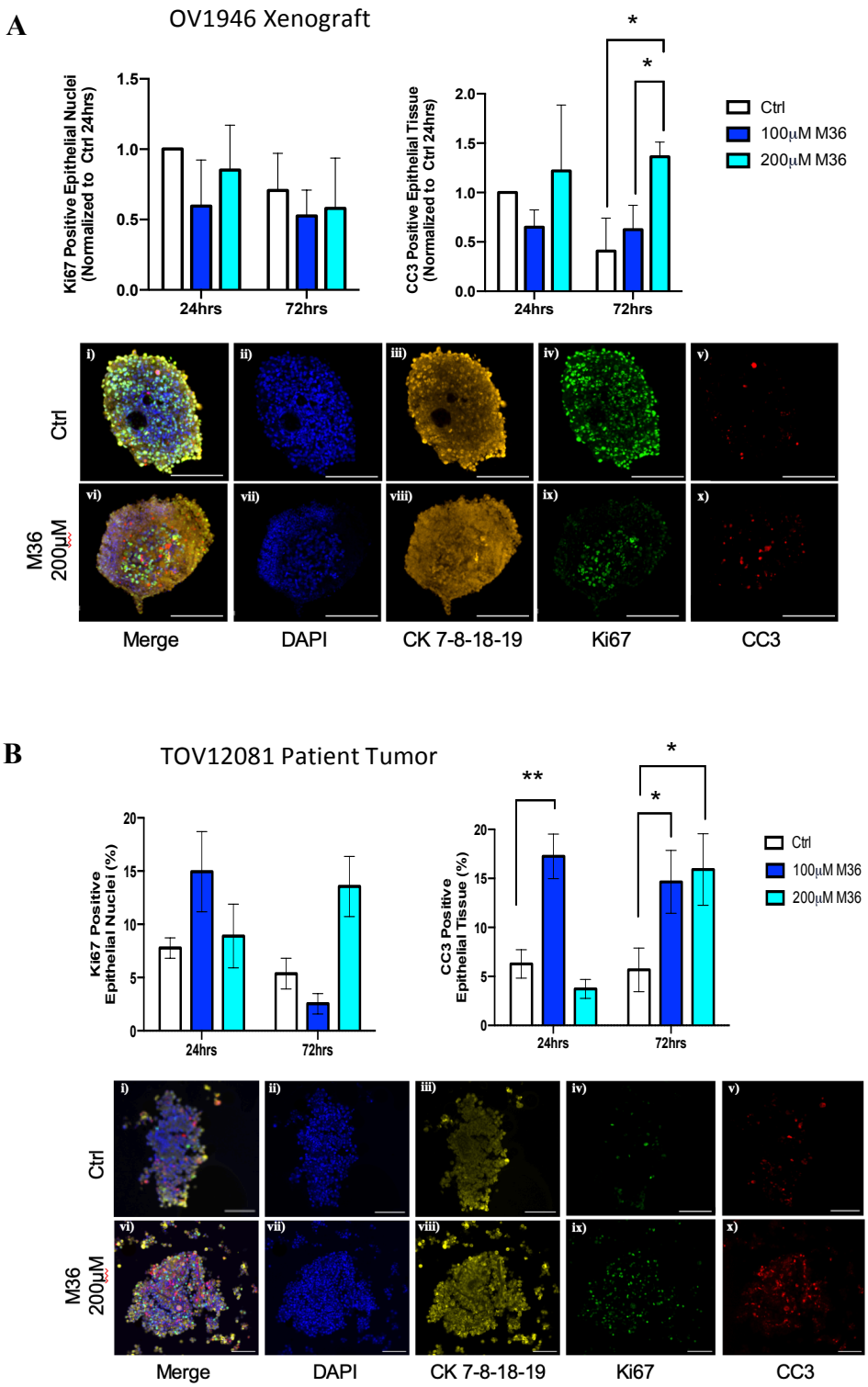

577

578 **Figure 6: M36 induces cell death of *ex vivo* micro-dissected tumors from xenografts and**

579 **patients**

580 Samples from OV1946 xenografts **(A)** or TOV12018G patient tumor **(B)** were processed as
581 micro-dissected tissues (MDTs) and cultured in microfluidic devices as described in Methods.
582 MDTs were treated with M36 at different concentrations for 24 or 72 h and then formalin-fixed,
583 paraffin embedded. Sections (6µ) were stained for KI67 (green), cleaved-caspase 3 (red), a
584 cytokeratin cocktail (yellow) and DAPI (blue). Bar graphs represent the expression of nuclear
585 KI67 (left panels) or CC3 (right panels) within the tumour epithelium (CK positive cells) of each
586 MDT. Data shown represents mean ± SEM of three separate experiments, normalized to Ctrl
587 24hrs. Statistical analysis was done using Two-way ANOVA followed by Tukey's test. *P <
588 0.05. Scale bars of representative images are 200 µm.
589

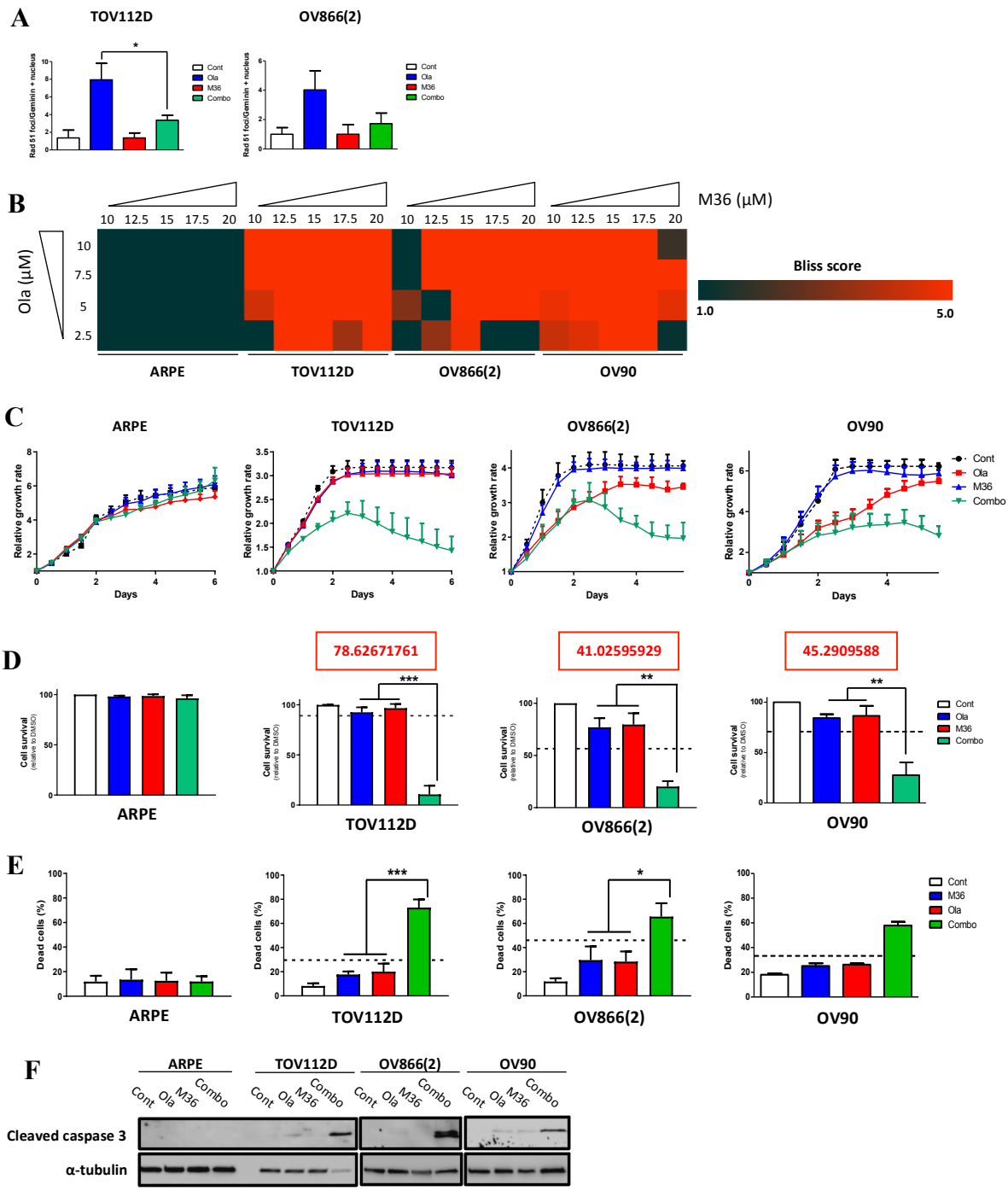

Figure 7: Combination of M36 and Olaparib triggers synthetic lethality in EOC cells

(A) TOV112D and OV866(2) cells were treated with M36 (20 μM) for 48 hours then with Olaparib (10 μM) for 24 hours. After fixation, cells were immunostained with Rad51 antibody. Quantitative analyses of foci formation are presented. **(B)** Cells were treated with increasing

595 concentrations of M36 and/or Olaparib. The heat map shows Bliss scores calculated for each
596 combination at day 6. **(C)** For each cell line, an example of proliferation profile following
597 Olaparib and M36 combination treatment is presented. **(D)** At the end of the experiment
598 presented in **(C)**, dead cells were removed by PBS washes and cell confluence was measured
599 using the live cell imaging IncuCyte system. Data are expressed as the percentage of control
600 cells. **(E, F)** ARPE and EOC cells were treated as in **(C)** and apoptosis was assessed by flow
601 cytometry **(E)** and western blot **(F)** using DRAQ7 dye and cleaved caspase 3 antibody,
602 respectively. *P < 0.05 **P < 0.01 *** P < 0.001 (n = 3. Student's t-test).

603

604

605 **REFERENCES**

606 1 Matchett, K. B. *et al.* Ran GTPase in nuclear envelope formation and cancer metastasis. *Adv Exp*
607 *Med Biol* **773**, 323-351, doi:10.1007/978-1-4899-8032-8_15 (2014).
608 2 Cavazza, T. & Vernos, I. The RanGTP Pathway: From Nucleo-Cytoplasmic Transport to Spindle
609 Assembly and Beyond. *Front Cell Dev Biol* **3**, 82, doi:10.3389/fcell.2015.00082 (2015).
610 3 Azuma, K. *et al.* Ran, a small GTPase gene, encodes cytotoxic T lymphocyte (CTL) epitopes
611 capable of inducing HLA-A33-restricted and tumor-reactive CTLs in cancer patients. *Clin*
612 *Cancer Res* **10**, 6695-6702, doi:10.1158/1078-0432.CCR-04-0818 (2004).
613 4 Ouellet, V. *et al.* Tissue array analysis of expression microarray candidates identifies markers
614 associated with tumor grade and outcome in serous epithelial ovarian cancer. *Int J Cancer* **119**,
615 599-607, doi:10.1002/ijc.21902 (2006).
616 5 Ouellet, V. *et al.* Discrimination between serous low malignant potential and invasive epithelial
617 ovarian tumors using molecular profiling. *Oncogene* **24**, 4672-4687, doi:10.1038/sj.onc.1208214
618 (2005).
619 6 Abe, H. *et al.* High expression of Ran GTPase is associated with local invasion and metastasis of
620 human clear cell renal cell carcinoma. *Int J Cancer* **122**, 2391-2397, doi:10.1002/ijc.23400
621 (2008).
622 7 Xia, F., Lee, C. W. & Altieri, D. C. Tumor cell dependence on Ran-GTP-directed mitosis. *Cancer*
623 *Res* **68**, 1826-1833, doi:10.1158/0008-5472.CAN-07-5279 (2008).
624 8 Yuen, H. F. *et al.* Ran is a potential therapeutic target for cancer cells with molecular changes
625 associated with activation of the PI3K/Akt/mTORC1 and Ras/MEK/ERK pathways. *Clin Cancer*
626 *Res* **18**, 380-391, doi:10.1158/1078-0432.CCR-11-2035 (2012).
627 9 Deng, L. *et al.* Ran GTPase protein promotes metastasis and invasion in pancreatic cancer by
628 deregulating the expression of AR and CXCR4. *Cancer Biol Ther* **15**, 1087-1093,
629 doi:10.4161/cbt.29217 (2014).
630 10 Sheng, C. *et al.* Knockdown of Ran GTPase expression inhibits the proliferation and migration of
631 breast cancer cells. *Mol Med Rep* **18**, 157-168, doi:10.3892/mmr.2018.8952 (2018).

632 11 Boudhraa, Z., Carmona, E., Provencher, D. & Mes-Masson, A. M. Ran GTPase: A Key Player in
633 Tumor Progression and Metastasis. *Front Cell Dev Biol* **8**, 345, doi:10.3389/fcell.2020.00345
634 (2020).
635 12 Harousseau, J. L., Shaughnessy, J., Jr. & Richardson, P. Multiple myeloma. *Hematology Am Soc*
636 *Hematol Educ Program*, 237-256, doi:10.1182/asheducation-2004.1.237 (2004).
637 13 Hartmann, E. *et al.* Five-gene model to predict survival in mantle-cell lymphoma using frozen or
638 formalin-fixed, paraffin-embedded tissue. *J Clin Oncol* **26**, 4966-4972,
639 doi:10.1200/JCO.2007.12.0410 (2008).
640 14 Schnepp, R. W. *et al.* A LIN28B-RAN-AURKA Signaling Network Promotes Neuroblastoma
641 Tumorigenesis. *Cancer Cell* **28**, 599-609, doi:10.1016/j.ccell.2015.09.012 (2015).
642 15 Cekan, P. *et al.* RCC1-dependent activation of Ran accelerates cell cycle and DNA repair,
643 inhibiting DNA damage-induced cell senescence. *Mol Biol Cell* **27**, 1346-1357,
644 doi:10.1091/mbc.E16-01-0025 (2016).
645 16 Kurisetty, V. V. *et al.* RAN GTPase is an effector of the invasive/metastatic phenotype induced
646 by osteopontin. *Oncogene* **27**, 7139-7149, doi:10.1038/onc.2008.325 (2008).
647 17 Ly, T. K. *et al.* Activation of the Ran GTPase is subject to growth factor regulation and can give
648 rise to cellular transformation. *J Biol Chem* **285**, 5815-5826, doi:10.1074/jbc.M109.071886
649 (2010).
650 18 Xia, F., Canovas, P. M., Guadagno, T. M. & Altieri, D. C. A survivin-ran complex regulates
651 spindle formation in tumor cells. *Mol Cell Biol* **28**, 5299-5311, doi:10.1128/MCB.02039-07
652 (2008).
653 19 Yuen, H. F. *et al.* Ran GTPase promotes cancer progression via Met recepto-rmediated
654 downstream signaling. *Oncotarget* **7**, 75854-75864, doi:10.18632/oncotarget.12420 (2016).
655 20 Yuen, H. F. *et al.* RanGTPase: a candidate for Myc-mediated cancer progression. *J Natl Cancer*
656 *Inst* **105**, 475-488, doi:10.1093/jnci/djt028 (2013).
657 21 Zaoui, K. *et al.* Ran promotes membrane targeting and stabilization of RhoA to orchestrate
658 ovarian cancer cell invasion. *Nat Commun* **10**, 2666, doi:10.1038/s41467-019-10570-w (2019).
659 22 Barres, V. *et al.* An essential role for Ran GTPase in epithelial ovarian cancer cell survival. *Mol*
660 *Cancer* **9**, 272, doi:10.1186/1476-4598-9-272 (2010).
661 23 Boudhraa, Z. *et al.* NR1D1 regulation by Ran GTPase via miR4472 identifies an essential
662 vulnerability linked to aneuploidy in ovarian cancer. *Oncogene* **41**, 309-320, doi:10.1038/s41388-
663 021-02082-z (2022).
664 24 Deng, L. *et al.* Ran GTPase protein promotes human pancreatic cancer proliferation by
665 deregulating the expression of Survivin and cell cycle proteins. *Biochem Biophys Res Commun*
666 **440**, 322-329, doi:10.1016/j.bbrc.2013.09.079 (2013).
667 25 Torre, L. A. *et al.* Ovarian cancer statistics, 2018. *CA Cancer J Clin* **68**, 284-296,
668 doi:10.3322/caac.21456 (2018).
669 26 Siegel, R. L., Miller, K. D., Fuchs, H. E. & Jemal, A. Cancer Statistics, 2021. *CA Cancer J Clin*
670 **71**, 7-33, doi:10.3322/caac.21654 (2021).
671 27 Lheureux, S., Gourley, C., Vergote, I. & Oza, A. M. Epithelial ovarian cancer. *Lancet* **393**, 1240-
672 1253, doi:10.1016/S0140-6736(18)32552-2 (2019).
673 28 Bashashati, A. *et al.* Distinct evolutionary trajectories of primary high-grade serous ovarian
674 cancers revealed through spatial mutational profiling. *J Pathol* **231**, 21-34, doi:10.1002/path.4230
675 (2013).
676 29 Lheureux, S., Braunstein, M. & Oza, A. M. Epithelial ovarian cancer: Evolution of management
677 in the era of precision medicine. *CA Cancer J Clin* **69**, 280-304, doi:10.3322/caac.21559 (2019).
678 30 Cancer Genome Atlas Research, N. Integrated genomic analyses of ovarian carcinoma. *Nature*
679 **474**, 609-615, doi:10.1038/nature10166 (2011).
680 31 Patch, A. M. *et al.* Whole-genome characterization of chemoresistant ovarian cancer. *Nature* **521**,
681 489-494, doi:10.1038/nature14410 (2015).

682 32 Scheffzek, K., Klebe, C., Fritz-Wolf, K., Kabsch, W. & Wittinghofer, A. Crystal structure of the
683 nuclear Ras-related protein Ran in its GDP-bound form. *Nature* **374**, 378-381,
684 doi:10.1038/374378a0 (1995).
685 33 Stewart, M., Kent, H. M. & McCoy, A. J. Structural basis for molecular recognition between
686 nuclear transport factor 2 (NTF2) and the GDP-bound form of the Ras-family GTPase Ran. *J Mol*
687 *Biol* **277**, 635-646, doi:10.1006/jmbi.1997.1602 (1998).
688 34 Chook, Y. M. & Blobel, G. Structure of the nuclear transport complex karyopherin-beta2-Ran x
689 GppNHp. *Nature* **399**, 230-237, doi:10.1038/20375 (1999).
690 35 Vetter, I. R., Arndt, A., Kutay, U., Gorlich, D. & Wittinghofer, A. Structural view of the Ran-
691 Importin beta interaction at 2.3 A resolution. *Cell* **97**, 635-646, doi:10.1016/s0092-
692 8674(00)80774-6 (1999).
693 36 Vetter, I. R., Nowak, C., Nishimoto, T., Kuhlmann, J. & Wittinghofer, A. Structure of a Ran-
694 binding domain complexed with Ran bound to a GTP analogue: implications for nuclear
695 transport. *Nature* **398**, 39-46, doi:10.1038/17969 (1999).
696 37 Ostrem, J. M., Peters, U., Sos, M. L., Wells, J. A. & Shokat, K. M. K-Ras(G12C) inhibitors
697 allosterically control GTP affinity and effector interactions. *Nature* **503**, 548-551,
698 doi:10.1038/nature12796 (2013).
699 38 McGregor, L. M., Jenkins, M. L., Kerwin, C., Burke, J. E. & Shokat, K. M. Expanding the Scope
700 of Electrophiles Capable of Targeting K-Ras Oncogenes. *Biochemistry* **56**, 3178-3183,
701 doi:10.1021/acs.biochem.7b00271 (2017).
702 39 Li, B. *et al.* Butyrylcholinesterase, paraoxonase, and albumin esterase, but not carboxylesterase,
703 are present in human plasma. *Biochem Pharmacol* **70**, 1673-1684, doi:10.1016/j.bcp.2005.09.002
704 (2005).
705 40 Martinez Molina, D. *et al.* Monitoring drug target engagement in cells and tissues using the
706 cellular thermal shift assay. *Science* **341**, 84-87, doi:10.1126/science.1233606 (2013).
707 41 Zeng, Y., Arisa, O., Peer, C. J., Fojo, A. & Figg, W. D. PARP inhibitors: A review of the
708 pharmacology, pharmacokinetics, and pharmacogenetics. *Semin Oncol* **51**, 19-24,
709 doi:10.1053/j.seminoncol.2023.09.005 (2024).
710 42 Levine, M. S. *et al.* Centrosome Amplification Is Sufficient to Promote Spontaneous
711 Tumorigenesis in Mammals. *Dev Cell* **40**, 313-322 e315, doi:10.1016/j.devcel.2016.12.022
712 (2017).
713 43 Charames, G. S. & Bapat, B. Genomic instability and cancer. *Curr Mol Med* **3**, 589-596,
714 doi:10.2174/1566524033479456 (2003).
715 44 Clarke, P. R., Klebe, C., Wittinghofer, A. & Karsenti, E. Regulation of Cdc2/cyclin B activation
716 by Ran, a Ras-related GTPase. *J Cell Sci* **108 (Pt 3)**, 1217-1225, doi:10.1242/jcs.108.3.1217
717 (1995).
718 45 Brodeur, M. N. *et al.* Carboplatin response in preclinical models for ovarian cancer: comparison
719 of 2D monolayers, spheroids, ex vivo tumors and in vivo models. *Sci Rep* **11**, 18183,
720 doi:10.1038/s41598-021-97434-w (2021).
721 46 Simeone, K. *et al.* Paraffin-embedding lithography and micro-dissected tissue micro-arrays: tools
722 for biological and pharmacological analysis of ex vivo solid tumors. *Lab Chip* **19**, 693-705,
723 doi:10.1039/c8lc00982a (2019).
724 47 Lord, C. J. & Ashworth, A. BRCAness revisited. *Nat Rev Cancer* **16**, 110-120,
725 doi:10.1038/nrc.2015.21 (2016).
726 48 Bansal, M. *et al.* A community computational challenge to predict the activity of pairs of
727 compounds. *Nat Biotechnol* **32**, 1213-1222, doi:10.1038/nbt.3052 (2014).
728 49 Xia, Y. *et al.* Increased miR-203-3p and reduced miR-21-5p synergistically inhibit proliferation,
729 migration, and invasion in esophageal cancer cells. *Anticancer Drugs* **30**, 38-45,
730 doi:10.1097/CAD.0000000000000687 (2019).
731 50 Dakir, E. H. *et al.* The anti-psychotic drug pimozide is a novel chemotherapeutic for breast
732 cancer. *Oncotarget* **9**, 34889-34910, doi:10.18632/oncotarget.26175 (2018).

733 51 Anzalone, A. *et al.* Dual control of dopamine synthesis and release by presynaptic and
734 postsynaptic dopamine D2 receptors. *J Neurosci* **32**, 9023-9034, doi:10.1523/JNEUROSCI.0918-
735 12.2012 (2012).
736 52 Sharma, A., McCarron, P., Matchett, K., Hawthorne, S. & El-Tanani, M. Anti-Invasive and Anti-
737 Proliferative Effects of shRNA-Loaded Poly(Lactide-Co-Glycolide) Nanoparticles Following
738 RAN Silencing in MDA-MB231 Breast Cancer Cells. *Pharm Res* **36**, 26, doi:10.1007/s11095-
739 018-2555-6 (2018).
740 53 Haggag, Y. A. *et al.* Nano-encapsulation of a novel anti-Ran-GTPase peptide for blockade of
741 regulator of chromosome condensation 1 (RCC1) function in MDA-MB-231 breast cancer cells.
742 *Int J Pharm* **521**, 40-53, doi:10.1016/j.ijpharm.2017.02.006 (2017).
743 54 Haggag, Y. A. *et al.* Novel Ran-RCC1 Inhibitory Peptide-Loaded Nanoparticles Have Anti-
744 Cancer Efficacy In Vitro and In Vivo. *Cancers (Basel)* **11**, doi:10.3390/cancers11020222 (2019).
745 55 Desai, N. Challenges in development of nanoparticle-based therapeutics. *AAPS J* **14**, 282-295,
746 doi:10.1208/s12248-012-9339-4 (2012).
747 56 Haley, B. & Frenkel, E. Nanoparticles for drug delivery in cancer treatment. *Urol Oncol* **26**, 57-
748 64, doi:10.1016/j.urolonc.2007.03.015 (2008).
749 57 Fang, Z., Grutter, C. & Rauh, D. Strategies for the selective regulation of kinases with allosteric
750 modulators: exploiting exclusive structural features. *ACS Chem Biol* **8**, 58-70,
751 doi:10.1021/cb300663j (2013).
752 58 Kim, G. *et al.* FDA Approval Summary: Olaparib Monotherapy in Patients with Deleterious
753 Germline BRCA-Mutated Advanced Ovarian Cancer Treated with Three or More Lines of
754 Chemotherapy. *Clin Cancer Res* **21**, 4257-4261, doi:10.1158/1078-0432.CCR-15-0887 (2015).
755 59 Drean, A., Lord, C. J. & Ashworth, A. PARP inhibitor combination therapy. *Crit Rev Oncol*
756 *Hematol* **108**, 73-85, doi:10.1016/j.critrevonc.2016.10.010 (2016).
757 60 O'Sullivan Coyne, G., Chen, A. P., Meehan, R. & Doroshow, J. H. PARP Inhibitors in
758 Reproductive System Cancers: Current Use and Developments. *Drugs* **77**, 113-130,
759 doi:10.1007/s40265-016-0688-7 (2017).
760 61 Fleury, H. *et al.* Cumulative defects in DNA repair pathways drive the PARP inhibitor response
761 in high-grade serous epithelial ovarian cancer cell lines. *Oncotarget* **8**, 40152-40168,
762 doi:10.18632/oncotarget.10308 (2017).
763 62 Ouellet, V. *et al.* Characterization of three new serous epithelial ovarian cancer cell lines. *BMC*
764 *Cancer* **8**, 152, doi:10.1186/1471-2407-8-152 (2008).
765 63 Fleury, H. *et al.* Novel high-grade serous epithelial ovarian cancer cell lines that reflect the
766 molecular diversity of both the sporadic and hereditary disease. *Genes Cancer* **6**, 378-398 (2015).
767 64 Letourneau, I. J. *et al.* Derivation and characterization of matched cell lines from primary and
768 recurrent serous ovarian cancer. *BMC Cancer* **12**, 379, doi:10.1186/1471-2407-12-379 (2012).
769 65 Provencher, D. M. *et al.* Characterization of four novel epithelial ovarian cancer cell lines. *In*
770 *Vitro Cell Dev Biol Anim* **36**, 357-361, doi:10.1290/1071-
771 2690(2000)036<0357:COFNEO>2.0.CO;2 (2000).
772 66 Astolfi, M. *et al.* Micro-dissected tumor tissues on chip: an ex vivo method for drug testing and
773 personalized therapy. *Lab Chip* **16**, 312-325, doi:10.1039/c5lc01108f (2016).

774